1 **PET imaging of neutrophil elastase with ^{11}C-GW457427 in Acute Respiratory Distress**

2 **Syndrome in pigs**

3 **Authors:** Emmi Puuvuori[1], Elena Chiodaroli[2], Sergio Estrada[1], Pierre Cheung[1], Norbert Lubenow[3],

4 Jonathan Sigfridsson[4], Hampus Romelin[4], Sofie Ingvast[3], Mathias Elgland[1,4], Francesco Liggieri[2],

5 Olle Korsgren[3], Gaetano Perchiazzi[2*], Olof Eriksson[1*], Gunnar Antoni[1,4*]

6 Affiliations:

7 [1] Science for Life Laboratory, Department of Medicinal Chemistry, Uppsala University, Uppsala,

8 Sweden

9 [2] The Hedenstierna Laboratory, Department of Surgical Sciences, Uppsala University, Uppsala

10 Sweden

11 [3] Department of Immunology, Genetics and Pathology, Uppsala University, Uppsala, Sweden

12 [4] PET Center, Center for Medical Imaging, Uppsala University Hospital, Uppsala, Sweden

13 * Senior authors, contributed equally

14

15 **First author:**

16 Emmi Puuvuori

17 Science for Life Laboratory, Department of Medicinal Chemistry, Uppsala University

18 Dag Hammarskjöldsv 14C, 3rd floor

19 75183 Uppsala, Sweden

20 +358-503726382

21 Email: emmi.puuvuori@ilk.uu.se

22

23 **Corresponding authors:**

24 Olof Eriksson

25 Science for Life Laboratory, Department of Medicinal Chemistry, Uppsala University

26 Dag Hammarskjöldsv 14C, 3rd floor

27 75183 Uppsala, Sweden

28 +46-707903054

29 Email: olof.eriksson@ilk.uu.se

30

31 Gunnar Antoni, Adj. Prof.

32 Department of Medicinal Chemistry, Uppsala University,

33 PET-Centre Uppsala University Hospital,

1   SE-75185 Uppsala, Sweden

2   +46705480305

3   Email: gunnar.antoni@akademiska.se

4

5   **Word count:** 4984

6   **Figures:** 3 (+ 4 Supplementary figures)

7   **Short title:** PET imaging of neutrophil elastase

8

1 **ABSTRACT**

2 Today, there is a lack of clinically available imaging techniques to detect and quantify specific

3 immune cell populations. Neutrophils are one of the first immune cells at the site of inflammation

4 and they secrete the serine protease neutrophil elastase (NE), which is crucial in the fight against

5 pathogens. However, the prolonged lifespan of neutrophils increases the risk for patients to develop

6 severe complications, such as Acute Respiratory Distress Syndrome (ARDS). Here, we evaluated

7 novel radiolabeled NE inhibitor ^{11}C-GW457427 in a pig model of ARDS, for detection and

8 quantification of neutrophil activity in the lungs.

9 **Methods:** ARDS was induced by intravenous administration of oleic acid on 5 farm pigs and 4 were

10 considered as healthy controls. The severity of ARDS was monitored by clinical parameters of lung

11 function and plasma biomarkers. Each pig was studied with ^{11}C-GW457427 and PET-CT, before and

12 after pretreatment with the NE inhibitor GW311616 to determine in vivo binding specificity. PET

13 image data was analyzed as Standard Uptake Values (SUV) and correlated to immunohistochemical

14 staining for NE in biopsies.

15 **Results:** The binding of ^{11}C-GW457427 was increased in pig lungs with induced ARDS (median

16 SUV_{mean}= 1.91, inter-quartile range (IQR) = 1.67-2.55) compared with healthy controls pigs (p

17 <0.05, p= 0.03, median SUV_{mean}=1.04, IQR= 0.66-1.47). The binding was especially strong in lung

18 regions with high levels of neutrophil elastase and ongoing inflammation, as verified by

19 immunohistochemistry. The binding was successfully blocked by pretreatment of a NE inhibitor

20 drug, which demonstrated the *in vivo* specificity of ^{11}C-GW457427 (p <0.05, p= 0.04, median

21 SUV_{mean}= 0.60, IQR= 0.58-0.77). The binding in neutrophil rich tissues such as bone marrow (p

22 <0.05, p=0.04, baseline median SUV_{mean}= 5.01, IQR= 4.48-5.49, block median SUV_{mean}= 1.57, IQR=

23 0.95-1.85) and spleen (median SUV_{mean}= 2.14, IQR= 1.19-2.36) was also high in all pigs.

24 **Conclusion:** ^{11}C-GW457427 binds to NE in a porcine model of oleic acid induced lung inflammation

25 in vivo with specific increase in regional lung, bone marrow, and spleen SUV. ^{11}C-GW457427 is a

26 promising tool for localizing, tracking and quantifying neutrophil facilitated inflammation in clinical

27 diagnostics and drug development.

28

29 **Keywords:** Inflammation, PET, neutrophil elastase, ARDS

30

1 **INTRODUCTION**

2 The acute respiratory distress syndrome (ARDS) is a life-threatening condition characterized by lung

3 injury, infiltration of immune cells, increased permeability and decreased pulmonary function (*1*).

4 Inflammation damages the thin-walled alveoli and the alveolar-capillary unit, determining lung

5 edema, decreased lung compliance and hypoxemia eventually resulting in the need for mechanical

6 ventilation (*2*). Different direct (e.g. pneumonia or pulmonary injury) or indirect mechanisms (e.g.

7 sepsis) can lead to ARDS and despite improvement in treatment, the condition is associated to high

8 mortality (*3*).

9

10 There are several inflammatory biomarkers associated with ARDS, such as cytokines,

11 demonstrating that immune cell recruitment and accumulation are an important path of the pathology

12 (*4*). Inflammatory processes may affect all major organs, and unresolved may lead to development of

13 fibrosis and finally organ failure. Even in ARDS induced by intra-pulmonary causes like injurious

14 mechanical ventilation, the activation of inflammatory cascade and mediators carried by blood

15 circulation can reach remote organs and contribute to multi-organ failure (*5*).

16 In this process, immune-active cells such as leukocytes play a key role and neutrophils are the

17 most abundant leukocytes in the circulation. They are part of the innate immune system acting as first

18 line of defense in the immune response and are recruited to the site of damage within minutes

19 following trauma or acute inflammation. Neutrophils are produced from stem cells in the bone

20 marrow, and they are highly mobile in the bloodstream, but also in the marginated intravascular pools

21 located in lungs, spleen, and liver (*6-7*). The lifespan of neutrophils in healthy humans is short lived

22 as inactivated neutrophils only survive around 8 hours (*8*). However, the activated neutrophils can

23 prolong their existence up to 5 days (*9*). The extended life of activated neutrophils promotes chronic

24 inflammation and inflammatory-related morbidity in several lung diseases, including ARDS (*7, 10*).

25 Upon activation, neutrophils can increase permeability of the blood vessels to proteins and migrate

26 through them into interstitium. Neutrophils can defend the host from invaders by phagocytosis,

27 secretion, and release of anti-microbials (degranulation) and formation of neutrophil extracellular

28 traps (NETs) (*11*). One of the biomarkers linked with ARDS include NETs, whose purpose is to

29 physically trap micro-organisms on the DNA-strands to prevent the spread and by disarming

30 pathogens using antimicrobial proteins such as neutrophil elastase (NE) (*2*).

31 NE is a serine protease stored in the primary granules of neutrophils and released upon

32 neutrophil activation by degranulation and NETs. Thus, NE has a key role in mediating tissue

33 remodeling, but it can also damage the lung parenchyma and the airway walls. NE inhibitors such as

Sivelestat[R] have been investigated as a treatment for acute lung injury and ARDS with mixed results without proven efficacy (*12*). This could potentially be explained by insufficient dosing/ exposure or duration of treatment. No quantitative molecular imaging modality such as positron emission tomography (PET) and a selective PET-tracer targeting NE has been used to verify the interaction between drug and drug target and quantify the degree of elastase inhibition *in vivo*. Thus, for the purpose of monitoring the potential of these novel therapeutic strategies, improved understanding, and techniques to monitor the disease progression non-invasively is required.

Currently the NE activity *in vivo* can be monitored by intravital microscopy, which is limited in depth and field of view and therefore mainly suitable for preclinical use on small animals (*6,13*). Clinically, *in vitro* NE levels can be analyzed from sputum and plasma samples; however, the sputum samples are unreliable and plasma samples are not tissue-specific to lungs.
In vivo imaging of NE activity has also been attempted, by radiolabeling of a peptide with high affinity for NE *(14)*. The resulting tracer ^{99m}Tc-MAG$_3$-EPI-HNE-2 could visualize inflammation in tissue in non-human primates, demonstrating the feasibility of NE in vivo imaging by Single Photon Emission Tomography (SPECT).
^{11}C-GW457427 (0.44kDa) is a novel small molecule PET tracer targeting neutrophil elastase. We have recently reported GMP ready production, toxicology, dosimetry, metabolite analysis and *in vivo* binding data in mouse for ^{11}C-GW457427 (*15*) as well as a pilot clinical study in patients with COVID-19 (*16*).

The aim of this study was to validate ^{11}C-GW457427 as a PET marker for NE in a translationally relevant large animal model of ARDS. Porcine and human neutrophils behave similarly and have comparable respiratory mechanics and gas exchange in the lungs (*17-18*). This makes the pig a relevant model for preclinical studies of NE in ARDS.

1 **MATERIALS AND METHODS**

2 **Radiosynthesis of ^{11}C-GW457427**

3   ^{11}C-GW457427 was synthesized as described in detail previously (*15-16*). ^{11}C-GW457427

4 (n=17) was generated with radiochemical purity of >95%.

5

6 **Animal Handling**

7   The animal experiments were authorized by the Animal Ethics Committee of the Swedish

8 Animal Welfare Agency and carried out according to the ARRIVE and institutional guidelines

9 ("Uppsala university guidelines on animal experimentation", UFV 2007/724).

10

11 **Induction of ARDS in Pig**

12   On the morning of the study day pigs (n=9, weight: 22-27 kg, Swedish landrace, mean age 2

13 months) were transported to Uppsala University and anesthetized initially by intramuscular

14 administration of tiletamine-zolazepam. Swedish Landrace pigs were chosen as they are a common

15 pig strain in Sweden. Their health is strictly controlled by the veterinarian authorities, but the strain is

16 not genetically modified or the result of inbreeding. The selected age of the pigs was primarily due to

17 logistics as Swedish Landrace pigs are around 25-30 kg in weight at the age of 2 months, which is

18 approaching a large enough size to be suitable for the spatial resolution of the clinical PET scanner

19 used (3-5 mm), while still being small enough to handle and transport under anaesthesia.

20

21   The anesthesia was maintained with intravenous ketamine, fentanyl and midazolam as

22 previously described (*19*). The experiment was conducted with the animal-in supine posture in order

23 to mimic a patient's position in the intensive care bed. The animals were ventilated in volume-

24 controlled mode, Inspired Oxygen Fraction (FiO_2) = 0.5, Positive End Expiratory Pressure =5

25 cmH_2O, Tidal Volume (V_T)=6 ml/kg, respiratory rate 20/min. Minute volume was adjusted to

26 maintain normocapnia during the course of the experiment by titrating the respiratory frequency.

27 Acute lung damage was induced in five pigs, by injection of oleic acid (cis-9-octadecenoic acid, OA)

28 as described previously in detail (*20-21*). Approximately 0.1 ml/kg OA-ethanol solution (1:1 by

29 volume) was given. OA-ethanol solution was administered through a central venous catheter in

30 repeated boluses of around 0.5 ml. Particular attention was paid to obtain a complete dispersion of

31 the OA into the infusate, avoiding large droplets. Administration of OA was suspended if O_2

32 saturation fell below 80%. Any fall in systemic arterial pressure during OA injection was countered

33 using epinephrine, in boluses of 0.01 mg.

1   Out of the nine pigs in this study, five were induced with lung inflammation and four were

2 untreated. The lung function and severity of the ARDS was evaluated by repeatedly monitoring

3 ventilator readouts (in particular lung compliance) and the partial pressure of arterial blood gases

4 together with the oxygen saturation of arterial haemoglobin (S_aO_2) and the ratio between P_aO_2

5 (partial pressure of oxygen in arterial blood) and FiO_2 (P/F ratio). The measurements were conducted

6 before the ARDS induction (baseline), directly after ARDS (T1), after the first injection of [11]C-

7 GW457427 (T2) and after the administration of blocking compound (T3).

8   Whole blood and plasma samples were also acquired at these time points, for analysis of

9 standard peripheral markers at the hospital clinical chemistry core lab. Blood samples were also

10 acquired for thromboelastography analysis of coagulation efficiency. The viscoelastic properties

11 were analyzed using the TEG 6 s® platform (Haemonetics, Boston, MA) (*22*), analyzing coagulation

12 in citrated whole blood, generating the parameters R-time (R), angle (A), maximal amplitude (MA),

13 and lysis at 30 min (Ly30(%)).

14

15 **[11]C-GW457427 PET-CT Imaging of Pigs with ARDS**

16   An attenuation CT scan (100 kV, 80-400 mA, noise index 10, rotation 0.5'', full spiral, slice

17 thickness 3.75 mm, pitch 0.98:1, recon diameter 50 mm) was initially attained using a digital 4-ring

18 system, 64-slice CT with a 198 mm axial field of view. Afterwards ^{11}C-GW457427 (10 MBq/kg,

19 corresponding to around 3-5 µg substance) was injected and a 60 min dynamic PET (Discovery MI,

20 GE Healthcare) scan (4 mm spatial resolution, 30 frames: 12x10s'', 6x30s'', 5x2min', 5x5min',

21 2x10min') was simultaneously started over the lungs. A 30 min static scan over the spleen was

22 immediately started after the dynamic study. Both scans were repeated after IV pretreatment of 1

23 mg/kg of NE inhibitor GW311616 (1 mL/kg of 1 mg/mL GW311616 in 0.9% NaCl), administered as

24 a slow bolus 20 min before the tracer, approximately 2 h after the first injection. The dose of inhibitor

25 (1 mg/kg) was based on the dosing used previously in mice (15) and was around 5000 times higher

26 than the tracer mass dose (in the range of 0.1-0.2 µg/kg).

27   The baseline scan was started approximately 2.5 h and the blocking scan 4.5 h after the OA

28 treatment was initiated. Radioactivity in arterial plasma and whole blood was determined during the

29 dynamic scans after 5min, 30min and 60min p.i. with a gamma well counter. Lastly, a contrast-

30 enhanced CT was acquired by late arterial (17 s) and venous phase contrast-enhanced CT (70 mL of

31 Omnipaque 350 + 40 mL NaCl, 3.5 mL/s, bolus tracking on descending aorta 100 HU threshold).

32 The reconstruction of PET images was done by using iterative VPFX-S algorithm (GE Healthcare;

OSEM, Time of Flight, Resolution recovery: 3 iterations, 16 subsets, 3 mm postfilter and 256x256 matrix).

After the PET scans, each pig was euthanized by intravenous KCl under deep anesthesia. Biopsies were taken from the lung (right and left, apical and basal parts), spleen and liver, both for snap freezing and fixation in formalin for immunohistochemical staining.

PET-CT Pig Image Data Analysis

The volumes of interest (VOIs) were manually segmented over the lungs as previously described in detail (*23*), on standard uptake value (SUV) corrected coronal projections using PMOD software (PMOD Technologies LLC, Zürich, Switzerland). No further kinetic modelling of PET data was performed, due to the lack of assessment of arterial metabolites in the pigs. The Hounsfield unit (HU) values over the lungs were obtained from CT images using same segmentations. In addition, bone and muscle VOIs were delineated on dynamic images and Time Activity Curves (TAC's) were defined on all organs. The data was summarized and illustrated on GraphPad Prism (GraphPad Software Inc., La Jolla, CA, USA) and presented as median and interquartile range (IQR). Baseline, blocking and control groups were tested for normality by Shapiro-Wilk test and since all groups were not normally distributed, the relationship between groups were assessed by Mann-Whitney U-test, where $p < 0.05$ was considered significant. None-significant relationships are marked as "ns".

Histology of Pig Biopsies

Formalin-fixed and paraffin-embedded biopsies of the lungs and spleen were acquired post-mortem following the PET studies and processed into 6 µm sections. Sections were immuno-stained for NE using an anti-Neutrophil Elastase antibody (ab68672, rabbit polyclonal, Abcam) in a concentration of 1 ug/ml. Bound antibody was visualized by Dako EnVision and diaminobenzidine (DAB)-based substrate (K4065, Agilent) according to the manufacturer's instructions. Sections were counterstained with hematoxylin, dehydrated, mounted and analyzed by light microscopy Leica. Pig spleen sections were used as positive control and negative controls had the primary antibody replaced by buffer. Consecutive sections from pig lung and spleen were also stained by Sirius Red (SIR) and Hematoxylin/ Eosin (H&E) according to routine at the local hospital pathology department (Uppsala University Hospital).

1 **RESULTS**

2 **Visual ^{11}C-GW457427 Uptake in ARDS pigs Compared to Control**

3   The neutrophil elastase infiltration after the lung damage was assessed using ^{11}C-GW457427

4 on pigs, in comparison with healthy animals. PET/CT images (from 30-60 minutes post

5 administration) as well as time activity curves displayed distinct uptake of ^{11}C-GW457427 in the

6 lungs of pigs with induced ARDS (Figure 1A and 1E), which was abolished in the second scan by

7 pretreatment with a NE inhibitor (Figure 1B and 1F). Conversely, lung uptake in control pigs was

8 negligible (Figure 1C-D and 1G-H). The binding ^{11}C-GW457427 in lung was consistent with positive

9 immunostaining for NE in lung from pig with induced ARDS (Supplemental Figure 1). Binding of

10 ^{11}C-GW457427 in the bone marrow was visible in both ARDS and control pigs, and the binding

11 could be blocked by pretreatment with a NE inhibitor (Figure 1A-H).

12

13 **Lung Binding of ^{11}C-GW457427 and ARDS Severity Assessment**

14   On the more damaged dorsal parts the uptake of [^{11}C]GW457427 was significantly higher at

15 baseline (median SUV_{mean}= 1.91, IQR= 1.67-2.55) compared with after preblocking (p <0.05, p=

16 0.04, median SUV_{mean}= 0.60, IQR= 0.58-0.77) and control pigs (p <0.05, p= 0.03, median

17 SUV_{mean}=1.04, IQR= 0.66-1.47) at 60min p.i. (Figure 2A). The uptake on the ventral parts was also

18 significantly higher at baseline (median SUV_{mean}= 0.76, IQR= 0.63-0.98) compared with blocking (p

19 <0.05, p=0.04, median SUV_{mean}= 0.32, IQR= 0.27-0.47) but not between ARDS and healthy control

20 pig (p=0.41, median SUV_{mean}= 0.66, IQR= 0.47-0.89) (Figure 2A). The successful induction of

21 ARDS was confirmed by continuous monitoring of lung function (Figure 2B and Supplementary

22 Table 1). The P/F ratio decreased with time, dropping below 100 [mmHg] at T2, confirmed the

23 presence of severe ARDS according to the Berlin definition (*1*). The oxygen saturation dropped

24 longitudinally, having a significant difference (p<0.05, p= 0.02) between baseline and T3 (Figure

25 2B). The damage was also evident in the quantitative analysis of the CT (Figure 2C), where the most

26 dorsal parts of the lungs exhibited average density of -63.52 HU, compared with control dorsal (-

27 495.52 HU), baseline ventral (-528.00 HU) and the control ventral (-652.20 HU) parts. Common

28 clinical chemistry laboratory markers were also measured in repeated blood samples of each pig,

29 where changes in peripheral markers were inconclusive (Supplementary Figure 2).

30 Thromboelastography results under the experiments duration show no evidence of coagulopathy,

31 with no significant differences between the ARDS-group and control at baseline (Supplementary

32 Figure 3). Histological staining for NE, H/E and SIR in tissue biopsies taken post-mortem further

demonstrated severe inflammation in the lung of the ARDS group as well as NE positive cells in spleen (Supplementary Figure 1).

The plasma-to-whole-blood ratio for ^{11}C-GW457427 was examined in all the pigs throughout the dynamic studies. The plasma to blood ratio was below 1 in both ARDS induced pigs and control pigs after injection of tracer alone and decreased over time (Supplemental Figure 4A). After pre-blocking with a pharmacological dose of a NE inhibitor, the ration was instead above 1, and stable over the course of the PET scan, in both ARDS and control pigs. This indicates more ^{11}C-GW457427 available in plasma for tissue distribution, following pretreatment with the inhibitor.

Whole Body Distribution and Binding of [^{11}C]GW457427

The biodistribution seen in the static whole-body scans from 60-90 minutes after ^{11}C-GW457427 injection supported the finding for the dynamic PET scan. Strong ^{11}C-GW457427 binding was seen on both Maximum Intensity Projections (MIPs) (Figure 3A-B) and coronal projections (Supplemental Figure 4B-C) in hemopoietic tissues with known presence of neutrophils, including spleen, peripheral blood (here measured as heart ventricle) and bone marrow. Importantly, the binding in these tissues was decreased after inhibiting NE (Figure 3B-C, Supplemental Figure 4C). The presence of NE in pig spleen (median SUV_{mean}= 2.14, IQR= 1.19-2.36) was also verified by immunohistochemistry of paraffin embedded biopsies (Supplementary Figure 1). For example, the uptake in the bone marrow was significantly blocked ($p < 0.05$, p=0.04, baseline median SUV_{mean}= 5.01, IQR= 4.48-5.49, block median SUV_{mean}= 1.57, IQR= 0.95-1.85) on the ARDS model, and the binding to bone marrow in control animals (baseline median SUV_{mean}= 3.89, IQR= 2.49-4.23) was similar in magnitude to ARDS pigs. The muscle uptake remained unchanged on the background level (baseline median SUV_{mean}= 0.29, IQR= 0.27-0.34). Uptake in kidneys, liver and muscle was unaffected, consistent with non-specific uptake due to excretion or background blood contribution of the signal.

DISCUSSION

In this study we validated the novel radiotracer ^{11}C-GW457427 targeting NE in a large animal model of lung inflammation and ARDS. Neutrophils are the first cells migrating to the lungs during inflammation and their activation changes the lung pathology by releasing inflammatory mediators and molecules, such as NE. We demonstrated that the uptake of ^{11}C-GW457427 on an oleic acid induced lung inflammation model was strong, specific, and reproducible in pigs.

In both healthy and ARDS induced pigs the uptake of ^{11}C-GW457427 was heterogeneously distributed and higher in the more damaged dorsal (gravitationally dependent during the experiment) parts of the lungs. The spread of damage follows the distribution of lung circulation (*24*) and is supported by HU analysis and histology. In fact, both oleic acid and neutrophils are carried predominantly to the dependent, better perfused areas of the lung where it is possible to observe the multifocal and heterogenous alterations typical of ARDS (*25-26*). Since the lung injury models also cause permeability changes and vessel leakage, the risk for non-specific uptake gathering in the lungs is always present. However, in this study we were able to block the uptake of ^{11}C-GW457427 , indicating specificity of the binding and making us conclude that the dependent, dorsal areas of the lung are the real battleground where the inflammatory reaction takes place. The used tidal volumes, falling in the range of the so called "protective ventilation" (*27*) make us exclude a role of ventilator induced lung injury (*28*) in the present experiment.

In addition to the lungs, other organs of interest in this study consisted of hemopoietic tissues such as bone marrow and spleen. Since neutrophils are produced in the bone marrow, we expected to see uptake there as well as in spleen due the previously described accumulation in the marginated intravascular pools. The uptake was similar in ARDS and control pigs and the uptake of the tracer could be abolished, to a large extent by pretreatment with the selective NE inhibitor GW311616. Furthermore, we noticed binding in the blood pool, both by observing the signal in the heart ventricle (estimation of blood concentration), as well as by measuring the plasma and whole blood content of radioactivity in blood samples. During the baseline scan, where only ^{11}C-GW457427 was administered, there was a plasma-to-whole blood ratio lower than one, which decreased with time. This means that more ^{11}C-GW457427 was present in the cellular components than what was free in plasma. After pre-blocking with GW311616, the plasma-to-whole blood ratio increased to above one and was stable during the PET examination, indicating more tracer available in the plasma component. This was apparent both in the ARDS and control groups. We hypothesize that these observations are due to binding of ^{11}C-GW457427 to intracellular NE present in circulating neutrophils. The sum of data in hemopoietic tissue spleen, bone marrow and peripheral blood thus indicates the ^{11}C-GW457427 can cross the cell membrane of both activated and quiescent neutrophils and bind the intracellular pool of NE stored in granules. Such a NE specific binding in circulating neutrophils could also explain the weakly blockable signal observed also in the lung of control pigs, e.g. this signal is at least partially due to neutrophil continually passing though the tissue via the blood.

1   Analysis of the time dependent uptake in tissues from the dynamic scan showed that the

2   uptake remained stable in the lungs in ARDS but was slowly increasing in bone marrow during the

3   scan. NE, in circulating quiescent neutrophils and in the bone marrow, is stored in high condensed

4   granules, which are more inaccessible for binding to ^{11}C-GW457427 than NE that have been released

5   extracellularly to the tissue after activation/degranulation of the neutrophils at the site of

6   inflammation. The kinetics of binding of ^{11}C-GW457427 to extracellular, easily accessible NE will

7   likely be significantly faster, compared to binding to stored intracellular NE. To bind intracellular

8   NE, ^{11}C-GW457427 must diffuse through two membranes (both the cell and granule membranes) and

9   in addition the accessibility to the active site of NE could be reduced, due to the packing/storage of

10   the enzyme in the granules. This hypothesis would explain the difference in uptake kinetics (TAC) of

11   radioactivity in lung compared to that in bone marrow. Additionally, the observation of increased

12   whole blood-to-plasma ratio with time, in the baseline scans, also fits with this hypothesis.

13   Furthermore, we have preliminary data demonstrating that ^{11}C-GW457427 binds NE both in intact

14   and homogenized neutrophils (unpublished observations). Thus, ^{11}C-GW457427 will bind to both

15   extracellular activated NE, as well as intracellular inactivated NE inside neutrophils at the site of

16   inflammation. This is important information for correct interpretation of clinical ^{11}C-GW457427 PET

17   images, as it will be challenging to separate extracellular NE from neutrophils at sites of

18   inflammation. Further development to decrease the ability of ^{11}C-GW457427 to diffuse across the

19   cell membrane, e.g. by increasing hydrophilicity, may lead to a PET tracer more specific for

20   extracellular NE.

21   In lungs affected by ARDS and inflammation, the uptake is rapid and remains at a steady

22   level – in accordance with a fast on-rate of binding (k_{on}) due to the accessibility of NE. In the bone

23   marrow, on the other hand, overall kinetics are slower, and increasing during the duration of the scan

24   which is in accordance with an apparent slower k_{on} driven by the lower intracellular accessibility of

25   the target enzyme.

26

27   Previously, ^{18}F-Fluorodeoxyglucose (^{18}F-FDG) has been proposed as a potential marker to

28   assess neutrophilic recruitment in the lungs in inflammatory conditions. Even though neutrophils

29   contribute to the increased uptake of ^{18}F-FDG in lung inflammation, ^{18}F-FDG is inherently

30   nonspecific and will also accumulate in other activated immune cells with increased metabolism such

31   as macrophages, lymphocytes and eosinophils. The structural cells in the lungs also increase glucose

32   consumption throughout inflammation, contributing to the increased ^{18}F-FDG uptake. Therefore, [18]F-

33   FDG imaging represents the combined inflammatory response during lung inflammation and cannot

1   be reliably used to measure changes in specific immune cell populations e.g. neutrophilic

2   accumulation in response to e.g. anti-inflammatory treatments (*29-30*). ^{11}C-GW457427 belongs to a

3   class of selective NE inhibitors, originally developed for development as immunomodulatory drugs.

4   NE is highly specific for neutrophils, and it is thus unlikely that ^{11}C-GW457427 would bind to other

5   types of immune cells, such as macrophages.

6

7   The performance on ^{11}C-GW457427 in a large animal model of ARDS is in accordance with

8   previous data in rodents (*15*). In that study, strong lung binding of ^{11}C-GW457427 was seen in mice

9   after induction of lipopolysaccharide induction of lung inflammation, which could be blocked by co-

10   injection of 1 mg/kg unlabeled GW457427. Elevated signal was also found in spleen and bone

11   marrow, although not to the same extent as in pigs. The pig data presented here is furthermore in line

12   with the first in man results of ^{11}C-GW457427 with strong binding in inflammatory lesions in the

13   lung of individuals with COVID-19 but not controls (*16*). Additionally, strong binding was seen in

14   spleen and bone marrow in both groups – like in the pigs. The pig model has the added benefit of

15   allowing intervention by pre-administration of a NE inhibitor to demonstrate specificity of [11]C-

16   GW457427. Thus, the in vivo data presented here expands upon previous preclinical studies and

17   assist in interpretation of available and future clinical studies on ^{11}C-GW457427.

18

19   Limitations on the current study are mainly related to the experimental design, and the

20   restrictions on logistics imposed by the pig model. The strength of the experimental design is that it

21   allows direct comparison between the binding of the PET tracer in lung before and after blocking

22   with a NE inhibitor, in each individual. The drawback is instead that post-mortem assessment is only

23   available after the administration of inhibitor. Furthermore, the complexity and cost of the model and

24   its combination with the PET scanning, means that the number of repeated examinations in each

25   group is relatively low (n=3-5). Finally, the pigs are relatively young and may thus not accurately

26   recapitulate all aspects of the immune response in human adult ARDS.

27

28   In the future ^{11}C-GW457427 could potentially be used to demonstrate the pathophysiology of

29   damage distribution during ventilation-induced lung injury and patient self-induced lung injury

30   (which is still lacking direct morpho-functional proofs) (*31*) or to monitor the response to neutrophil-

31   targeting therapeutics during acute inflammation, e.g., Covid-19 treatments in drug development

32   (*32*). In fact, the recently reported first in man clinical study using ^{11}C-GW457427 did indeed

33   demonstrate strong binding in the lung of individuals with active COVID-19, indicating that NE

inhibitors may be a potential treatment strategy given the ample amount of NE in the inflammatory lesions. Neutrophils have also been found to accumulate in several types of tumors, making ^{11}C-GW457427 a potentially attractive non-invasive technique to be used to further elucidate the role of neutrophils and NE in immune oncology (*33-34*).

CONCLUSION

[11]C-GW457427 showed significantly higher uptake in a pig model of ARDS lung inflammation as compared with healthy pigs in vivo using PET. The specificity of ^{11}C-GW457427 binding to NE was verified by blocking studies with a NE inhibitor. ^{11}C-GW457427 is a promising and non-invasive tool for localizing, tracking and quantifying neutrophil mediated inflammation in clinical diagnostics and drug development.

AUTHOR CONTRIBUTIONS

E.P. designed the study, performed the research, data analysis, interpreted the data and wrote the manuscript; E.C. performed the research; S.E. performed the research; P.C. performed the research; N.L. designed the study and interpreted the data; J.S. performed the research; H.R. performed research; S.I. performed the research; M.E. performed the research; F.L. performed the research; O.K. designed the study and interpreted the data; G.P. designed the study, performed the research and interpreted the data; O.E. designed the study, performed the research, interpreted the data and wrote the manuscript, G.A. designed the study interpreted the data and wrote the manuscript. All authors reviewed, edited and approved the final version of the manuscript.

KEY POINTS

QUESTION: Can ^{11}C-GW457427 used to image neutrophil elastase in a large animal model?

PERTINENT FINDINGS: The preclinical evaluation of ^{11}C-GW457427 uptake in a pig lung inflammation model was consistent, reproducible and specific. The uptake in lung in pigs with ARDS was significantly increased compared with the healthy control animals and it could be abolished by preblocking.

IMPLICATIONS FOR PATIENT CARE: ^{11}C-GW457427 vis a novel PET tracer for in vivo imaging of Neutrophil Elastase, a crucial part of the innate immune system, in inflammatory diseases.

REFERENCES

1.   ARDS Definition Task Force, Ranieri VM, Rubenfeld GD, et al. Acute respiratory distress syndrome: the Berlin Definition. *JAMA*. 2012;307:2526-33

2.   Matthay MA, Zemans RL, Zimmerman GA, et al. Acute respiratory distress syndrome. *Nat Rev Dis Primers*. 2019;5:18.

3.   Bellani G, Laffey JG, Pham T, et al; LUNG SAFE Investigators; ESICM Trials Group. Epidemiology, patterns of care, and mortality for patients with acute respiratory distress syndrome in intensive care units in 50 countries. *JAMA*. 2016;315:788-800.

4.   Matthay MA, Ware LB, Zimmerman GA. The acute respiratory distress syndrome. *J Clin Invest*. 2012;122:2731-40.

5.   Plötz FB, Slutsky AS, van Vught AJ, Heijnen CJ. Ventilator-induced lung injury and multiple system organ failure: a critical review of facts and hypotheses. *Intensive Care Med*. 2004;30:1865-72.

6.   Silvestre-Roig C, Hidalgo A, Soehnlein O. Neutrophil heterogeneity: Implications for homeostasis and pathogenesis. *Blood*. 2016;127:2173-2181.

7.   De Filippo K, Rankin SM. The secretive life of neutrophils revealed by intravital microscopy. *Front Cell Dev Biol*. 2020;8:1-15.

8.   Summers C, Rankin SM, Condliffe AM, Singh N, Peters AM, Chilvers ER. Neutrophil kinetics in health and disease. *Trends Immunol*. 2010;31:318-324.

9.   Gramegna A, Amati F, Terranova L, et al. Neutrophil elastase in bronchiectasis. *Respir Res*. 2017;18:1-13.

10.   Williams AE, Chambers RC. The mercurial nature of neutrophils: still an enigma in ARDS? *Am J Physiol Lung Cell Mol Physiol*. 2014;306:L217-30.

11.   Klopf J, Brostjan C, Eilenberg W, Neumayer C. Neutrophil extracellular traps and their implications in cardiovascular and inflammatory disease. *Int J Mol Sci*. 2021;22:1-17.

12.   Iwata K, Doi A, Ohji G, et al. Effect of neutrophil elastase inhibitor (Sivelestat sodium) in the treatment of acute lung injury (ALI) and acute respiratory distress syndrome (ARDS): A systematic review and meta-analysis. *Intern Med*. 2010; 49:2423-2432

13. Fisher DT, Muhitch JB, Kim M, et al. Intraoperative intravital microscopy permits the study of human tumour vessels. *Nat Commun*. 2016;7:1-9.

14. Rusckowski M, Qu T, Pullman J, at al. Inflammation and infection imaging with a 99mTc-neutrophil elastase inhibitor in monkeys. *J Nucl Med*. 2000;41:363-74.

15. Estrada S, Elgland M, Selvaraju RK, et al. Preclinical evaluation of [11C]GW457427 as a tracer for neutrophil elastase. *Nucl Med Biol*. 2022;106-107:62-71.

16. Antoni G, Lubberink M, Sörensen J, et al. In vivo visualization and quantification of neutrophil elastase in lungs of COVID-19 Patients - a first-in-human positron emission tomography Study with ^{11}C-GW457427. *J Nucl Med*. 2022 Epub ahead of print. PMID: 35680418.

17. Bréa D, Meurens F, Dubois A V, et al. The pig as a model for investigating the role of neutrophil serine proteases in human inflammatory lung diseases. *Biochem J*. 2012;447:363-370.

18. Monteiro A, Smith RL. Bronchial tree Architecture in Mammals of Diverse Body Mass. I*nt J Morphol*. 2014;32:312-318.

19. Perchiazzi G, Rylander C, Derosa S, et al. Regional distribution of lung compliance by image analysis of computed tomograms. *Respir Physiol Neurobiol*. 2014;201:60-70.

20. Matute-Bello G, Frevert CW, Martin TR. Animal model of acute lung injury. *Am J Physiol Lung Cell Mol Physiol*. 2008;295:379–99

21. Perchiazzi G, Rylander C, Pellegrini M, Larsson A, Hedenstierna G. Monitoring of total positive end-expiratory pressure during mechanical ventilation by artificial neural networks. *J Clin Monit Comput*. 2017;31:551-559.

22. Dias JD, Haney EI, Mathew BA, Lopez-Espina CG, Orr AW, Popovsky MA. New-generation thromboelastography: comprehensive evaluation of citrated and heparinized blood sample storage effect on clot-forming variables. *Arch Pathol Lab Med*. 2017;141:569–577.

23. Puuvuori E, Liggieri F, Velikyan I, et al. PET-CT imaging of pulmonary inflammation using [68Ga]Ga-DOTA-TATE. *EJNMMI Res*. 2022;12:19.

24. Glenny RW, Robertson HT. Spatial distribution of ventilation and perfusion: mechanisms and regulation. *Compr Physiol*. 2011;1:375-95.

1 25. Gonçalves-de-Albuquerque CF, Silva AR, Burth P, et al. Acute Respiratory Distress

2 Syndrome: Role of Oleic Acid-Triggered Lung Injury and Inflammation. *Mediators Inflamm*.

3 2015;2015:260465.

4 26. Kamuf J, Garcia-Bardon A, Ziebart A, et al. Oleic acid-injection in pigs as a model for acute

5 respiratory distress syndrome. *J Vis Exp*. 2018;2018:1-8.

6 27. Acute Respiratory Distress Syndrome Network, Brower RG, Matthay MA, Morris A,

7 Schoenfeld D, Thompson BT, Wheeler A. Ventilation with lower tidal volumes as compared with

8 traditional tidal volumes for acute lung injury and the acute respiratory distress syndrome. *N Engl J*

9 *Med*. 2000;342:1301-8.

10 28. Slutsky AS, Ranieri VM. Ventilator-induced lung injury. *N Engl J Med*. 2013;369:2126-36.

11 29. Aulakh GK, Kaur M, Brown V, Ekanayake S, Khan B, Fonge H. Quantification of regional

12 murine ozone-induced lung inflammation using [18F]F-FDG microPET/CT imaging. *Sci Rep*.

13 2020;10:1-8.

14 30. Scherer PM, Chen DL. Imaging pulmonary inflammation. *J Nucl Med*. 2016;57:1764-1770.

15 31. Brochard L, Slutsky A, Pesenti A. Mechanical Ventilation to Minimize Progression of Lung

16 Injury in Acute Respiratory Failure. *Am J Respir Crit Care Med*. 2017;195:438-442.

17 32. Reusch N, De Domenico E, Bonaguro L, et al. Neutrophils in COVID-19. *Front Immunol*.

18 2021;12:1-9.

19 33. Uribe-Querol E, Rosales C. Neutrophils in cancer: two sides of the same coin. *J Immunol Res*.

20 2015;2015:983698.

21 34. Powell DR, Huttenlocher A. Neutrophils in the tumor microenvironment. *Trends Immunol*.

22 2016;37:41-52.

23
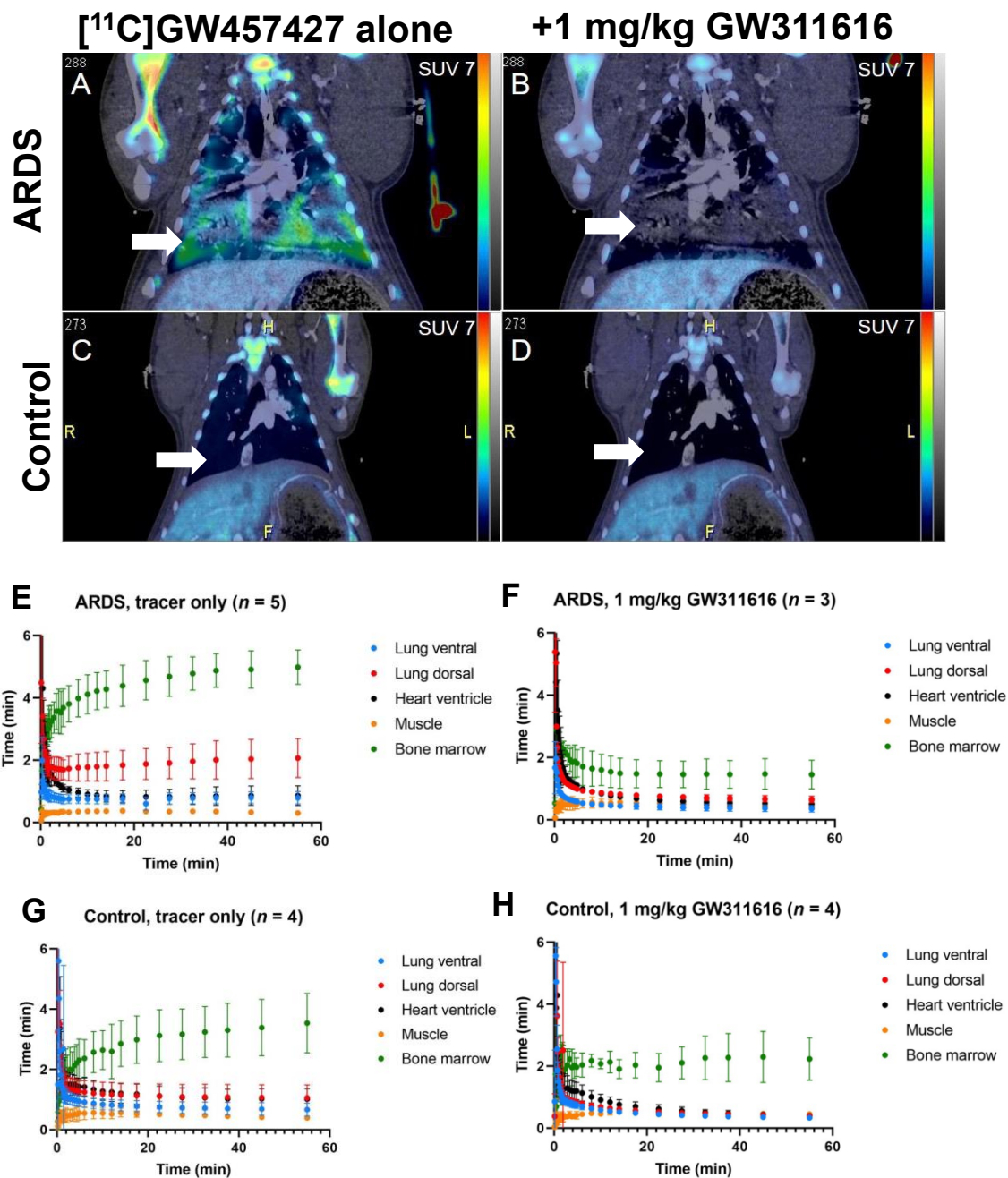
FIGURES

Figure 1. Representative PET-CT fused coronal images of the ARDS (top row, A-B) and control (bottom row, C-D) pigs after administration of ^{11}C-GW457427 alone or after pretreatment with NE inhibitor GW311616. White arrows indicate lungs and the SUV scale bar is from 0-7. The PET images are summed frames from 30-60 minutes post tracer administration. Averaged Time-Activity Curves showing the distribution and binding of ^{11}C-GW457427 in pigs with induced ARDS (E-F) and control pigs (G-H).
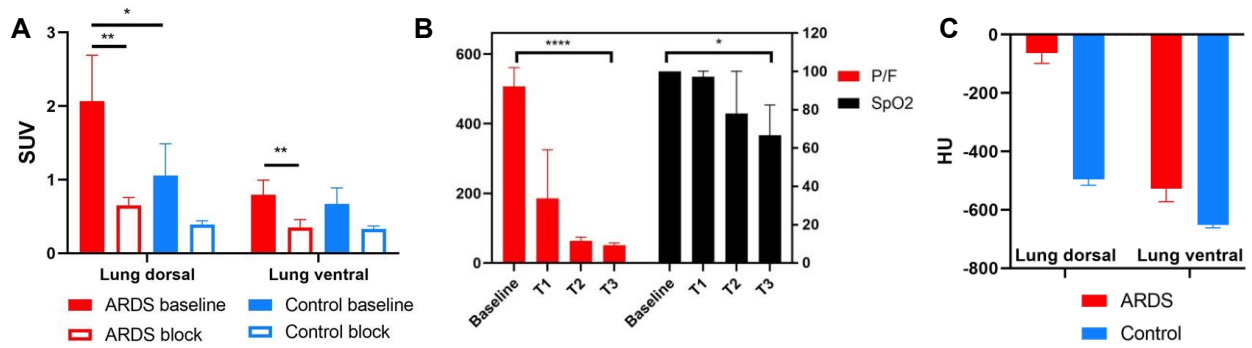
Figure 2. Binding of ^{11}C-GW457427 in lung regions in ARDS and control pigs (A). Lung function over time in the ARDS group, both before ARDS induction (baseline), directly after ARDS induction (T1), after the injection of ^{11}C-GW457427 (T2) and after the administration of blocking (T3) (B). The damage in the lungs in the ARDS model was clearly visible on CT, and was further confirmed by quantifying lung tissue density by CT (C).
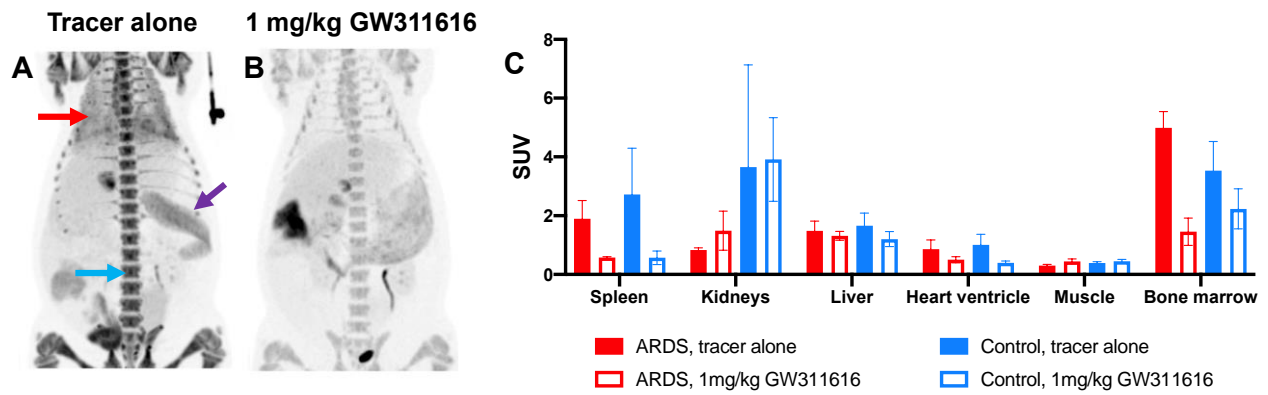
Figure 3. Representative images from the whole-body scan acquired from 60 to 90 minutes after ^{11}C-GW457427 administration. Maximum Intensity Projections (MIP) for baseline (A) and blocking (B) scans of the same pig. Red arrow indicate lung, purple arrow indicate spleen and blue arrow indicate bone marrow. Bar graph showing the binding of ^{11}C-GW457427 in tissues in both ARDS and control pigs during baseline scan or after blocking (C). Displaceable binding was found in spleen, heart ventricle and bone marrow.
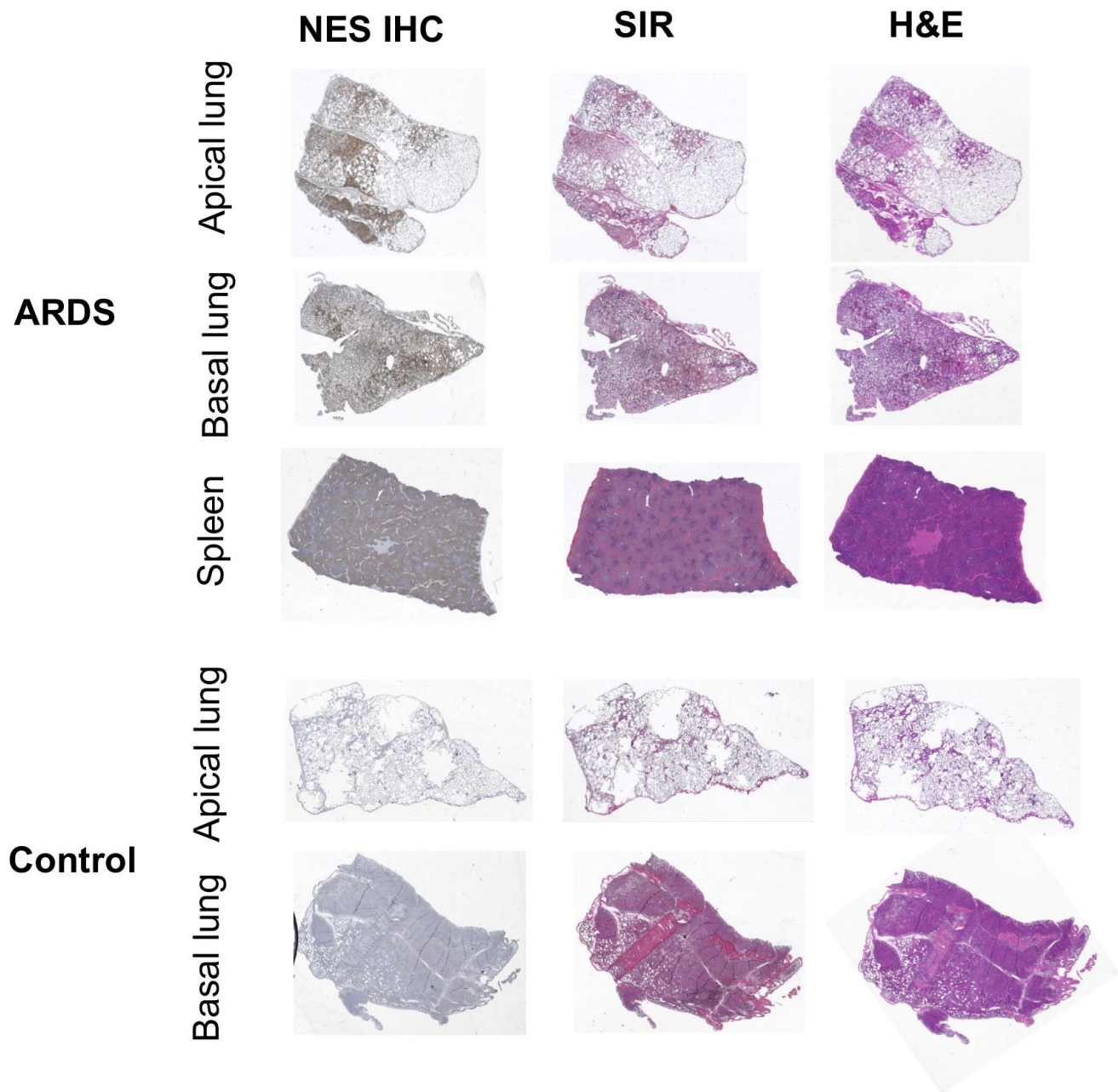
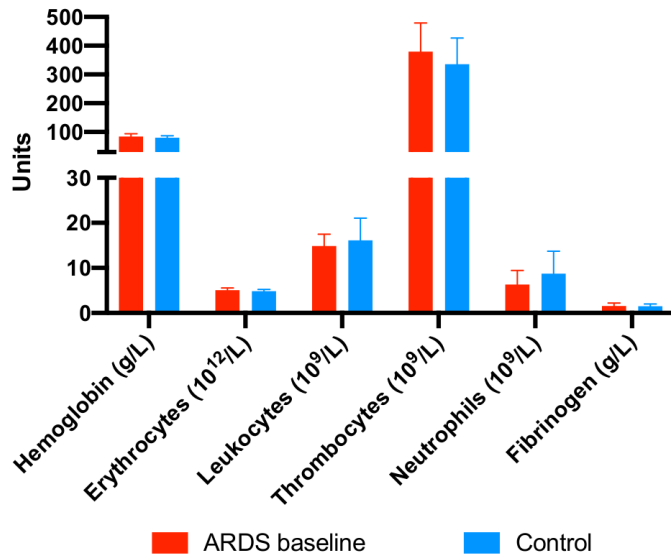1   **Graphical Abstract**
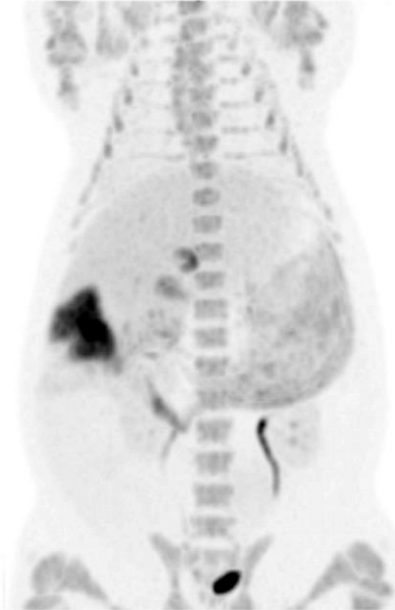
2
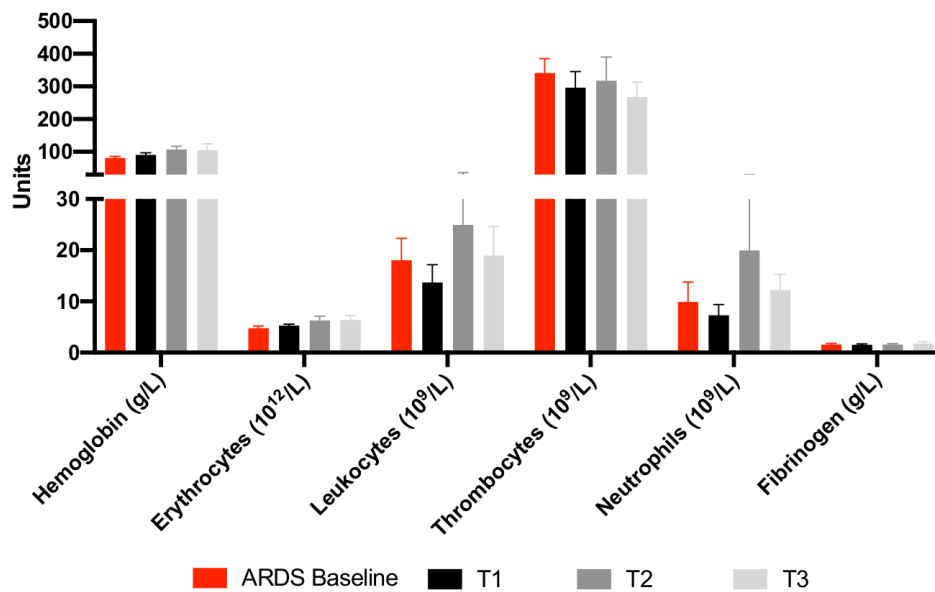
1 **SUPPLEMENTARY FIGURES**

2

3 **Supplementary Figure 1.** Representative immunohistological (IHC) staining for Neutrophil Elastase

4 (NE), as well as staining using Sirius Red (SIR) and Hematoxylin and Eosin (H&E), of lung and

5 spleen PFA biopsies from pigs with ARDS and controls.

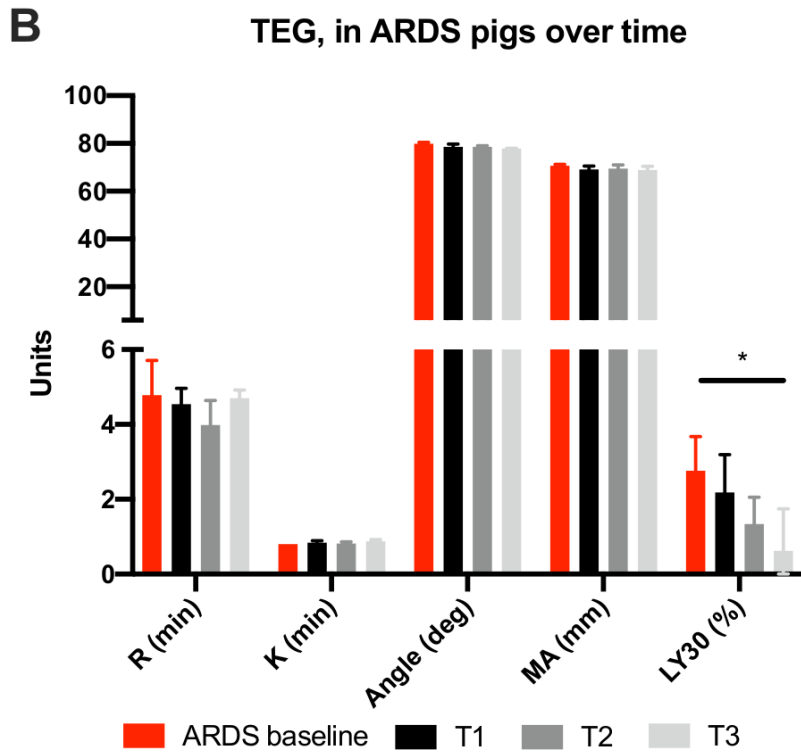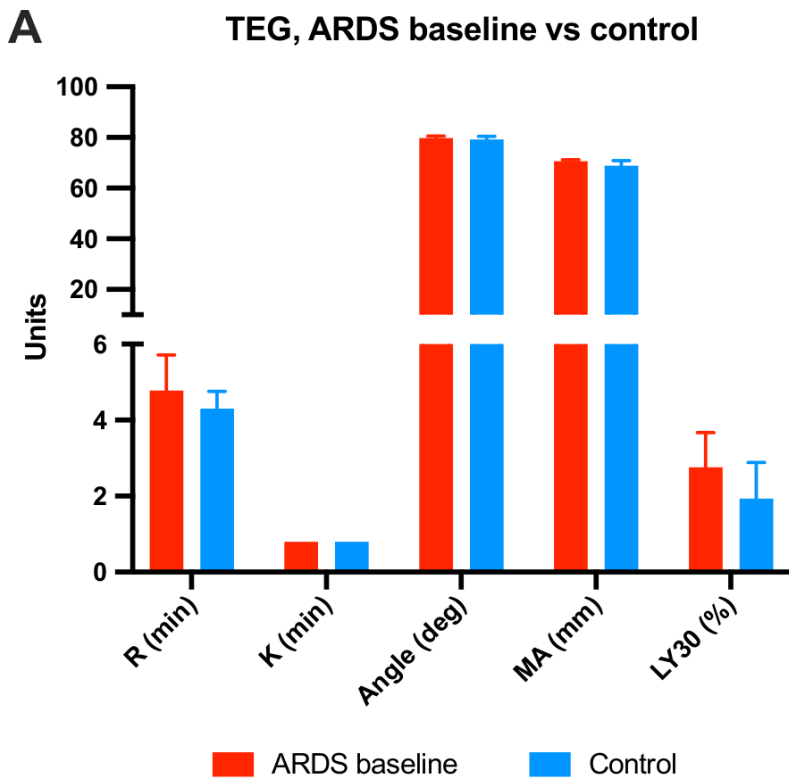**A**   **Plasma markers ARDS baseline vs controls**


B   **Plasma markers in ARDS pigs over time**

1

Supplementary Figure 2. The levels of common blood markers were similar in the pigs in both groups, before induction of ARDS (A). Change in plasma markers in the ARDS group, from before induction until the end of the experiment (B).

A TEG, ARDS baseline vs control

B TEG, in ARDS pigs over time

1

2   **Supplementary Figure 3.** Thromboelastography (TEG) readout in the pigs in both groups, before

3   induction of ARDS (A). Change in TEG readout in the ARDS group, from before induction until the

4   end of the experiment (B).

Tracer alone   1 mg/kg GW311616

1
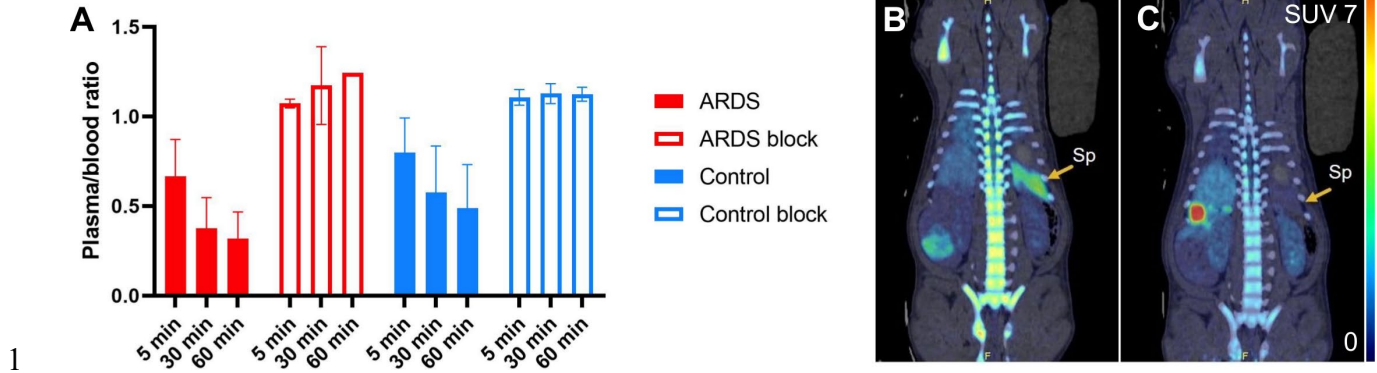
Supplementary Figure 4. Plasma to whole blood ratio of ^{11}C-GW457427 in pigs with ARDS and
control pigs, both after injection of tracer alone (filled bars) and after pretreatment with a NE
inhibitor (open bars) (A). Coronal projections of the whole-body scan at the level of the spleen after
administration of ^{11}C-GW457427 alone (B) or after pretreatment with NE inhibitor GW311616 (C).
Yellow single arrow and "Sp" indicates spleen.

1 **Supplementary Table 1.**

2 Overview on group level of assessment of ARDS severity, lung density (HU) and ^{11}C-GW457427

3 SUV uptake

Lung function	T0	T1	ARDS baseline T2	ARDS block T3	Control baseline T2	Control block T3
P/F	506.95	185.45	63.31	50.68	N/A	N/A
SpO$_2$	100	97.2	78	66.75	N/A	N/A
Lung dorsal (HU)			-63.52		-495.52	
Lung ventral (HU)			-528.01		-652.21	
^{11}C-GW457427 SUV$_{mean}$						
Lung dorsal			2.07	0.65	1.06	0.39
Lung ventral			0.79	0.35	0.67	0.33
Spleen			1.89	0.58	2.72	0.39
Kidneys			0.83	1.49	1.66	3.91
Liver			1.48	1.31	1.66	1.20
Heart ventricle			0.86	0.50	1.01	0.40
Muscle			0.30	0.44	0.39	0.45
Bone marrow			4.99	1.45	3.53	2.23

4